

1 **Title:** Electrical conductivity and grain boundary composition of Gd-doped and Gd/Pr co-doped
2 ceria

3 **Author names and affiliations:** William J. Bowman^a, Jiangtao Zhu^a, Renu Sharma^b, Peter A.
4 Crozier^a.

5 ^a School for the Engineering of Matter, Transport and Energy, Arizona State University, Tempe,
6 AZ 85287, USA. ^b Center for Nanoscale Science and Technology, National Institute of Standards
7 and Technology, Gaithersburg, MD 20899-6203, USA.

8 W.J.B – wjbowman@asu.edu, R.S. – renu.sharma@nist.gov, P.A.C. – crozier@asu.edu

9 **Corresponding author:** P.A.C. +001 (480) 965 2934

10 **ABSTRACT**

11 We characterize electrical conductivity, microstructure, nano-scale grain boundary structure and
12 chemistry of ceria electrolytes with nominal compositions of $\text{Gd}_{0.2}\text{Ce}_{0.8}\text{O}_{2-\delta}$ (GDC) and
13 $\text{Gd}_{0.11}\text{Pr}_{0.04}\text{Ce}_{0.85}\text{O}_{2-\delta}$ (GPDC). The electrolytes are fabricated using mixed oxide nanopowders
14 synthesized by spray drying. AC impedance spectroscopy was performed from 150 °C to 700 °C
15 in air to determine grain-interior electrical conductivity. Grain-boundary conductivity was
16 determined below 300 °C. The grain-interior conductivity of the GPDC was higher than that of
17 GDC by as much as 10 times, depending on the temperature. The GPDC specific grain-boundary
18 conductivity was measured to be approximately 100 times higher than that of GDC. Energy
19 dispersive x-ray spectroscopy (EDX) and electron energy-loss spectroscopy (EELS) in a
20 scanning transmission electron microscope (STEM) confirmed the grain-to-grain compositional
21 uniformity of both materials following heat treatments. Grain boundaries were free of glassy
22 intergranular phases; dopant concentration and Ce oxidation state was found to vary significantly
23 near grain boundaries. Boundary core composition was estimated from STEM EELS to be
24 $\text{Gd}_{0.62}\text{Ce}_{0.38}\text{O}_{2-\delta}$, and $\text{Gd}_{0.29}\text{Pr}_{0.16}\text{Ce}_{0.55}\text{O}_{2-\delta}$ in GDC and GPDC, respectively. Pr segregation to
25 grain boundaries in the GPDC is hypothesized to enhance conductivity by both decreasing
26 oxygen vacancy migration energy, and inducing mixed ionic-electronic conductivity in the near-
27 boundary region.

28 **KEYWORDS**

29 Doped ceria, spray drying, impedance spectroscopy, grain boundary, scanning transmission
30 electron microscopy, electron energy-loss spectroscopy.

31

32

33 **1. Introduction**

34 Intermediate temperature (350 °C to 550 °C) oxygen ion conductors and mixed ionic and
35 electronic conductors have received considerable attention in recent years due to their potential
36 applications in devices such as oxygen sensors, oxygen generators, separation membranes and
37 solid oxide fuel cells (SOFCs) [1-9]. Owing to its relatively high ionic conductivity under non-
38 reducing conditions and at intermediate temperatures, ceria doped with trivalent cations such as
39 Gd^{3+} or Sm^{3+} has emerged as a promising candidate material to provide the desired performance
40 in this operating temperature range. Other dopants such as mixed-valence $Pr^{3+/4+}$ induce
41 electronic conductivity yielding mixed ionic and electronic conductivity, an attractive possibility
42 for applications which require both electronic and ionic current. Furthermore, doubly-doping
43 with two cation species has been explored by experiment [2,5] and simulation [3]. For instance
44 Lubke et al. demonstrated increased electronic conductivity, and total ionic conductivity as the
45 result of decreased grain boundary resistance in Gd-doped ceria upon the addition of Pr [5]. This
46 result is in accordance with theoretical work based on density functional theory and Monte Carlo
47 simulations conducted by Dholobai et al. who predicted increased ionic conductivity in ceria
48 doped with both Pr and Gd [3].

49 The conductivity in a polycrystalline fluorite based oxide arises from conductivity through
50 grains and across grain boundaries. The grain boundaries are typically orders of magnitude less
51 conducting than the grain interior at intermediate temperatures. This reduced conductivity
52 originates from space-charge effects which hinder the transport of ions across the boundary [10].
53 Changes in the structure and composition may also have a substantial influence on the grain-
54 boundary conductivity. For example, formation of thin silica layers due to impurity segregation
55 to the grain boundary during heat treatment constricts the ion migration pathway, reducing the

56 electrical conductivity [10]. Conversely, segregation of some transition metals may reduce the
57 magnitude of the potential energy barrier at the grain boundary and enhance grain-boundary
58 conductivity [12]. The complex interplay between composition, structure and electrical
59 properties of grain boundaries is still not well understood. Understanding the role of nanoscale
60 structure and composition on grain-boundary electrical properties requires the correlation of
61 advanced transmission electron microscopy (TEM) with techniques such as impedance
62 spectroscopy. In this work, we employ AC impedance spectroscopy and high spatial resolution
63 TEM to investigate the electrical properties and nanoscale structure and chemistry of bulk
64 ceramics fabricated with spray-dried ceria doped with Gd, and doubly-doped with Gd and Pr.

65 A number of approaches have been employed to synthesize starting powders, or to
66 simultaneously synthesize starting materials and fabricate practical structures for the study of
67 solid ceramic electrolytes and electrodes. The overarching goal of these techniques is to fabricate
68 powders or device components with tunable chemistry and predictable microstructures which
69 provide the desired properties of the final component (e.g. high sintered density, ionic
70 conductivity and ionic transference for SOFC electrolytes). Researchers have reported using a
71 diverse set of synthesis approaches including co-precipitation [8], solid-state reactions [1,11,12],
72 spray pyrolysis [13], pulsed-laser deposition [14], DC sputtering [15], electrostatic spray
73 deposition [16], combustion and microwave syntheses [17] and aerosol deposition [18]. Due to
74 its simplicity, low cost, high yield, and ability to continuously produce nanoscale powders and
75 deposit layers of tunable composition, spray drying has also garnered attention for use in the
76 synthesis of several materials including rare-earth doped ceria [6,19-23]. During spray drying,
77 pressurized gas atomizes a liquid solution of precursor ions into a fine mist which enters a

78 reaction vessel where it is rapidly heated to produce solid solution particles that are
79 compositionally mixed at the nanometer scale.

80 An essential prerequisite of this work is to demonstrate that the spray drying method is an
81 effective approach for fabricating doped ceria model electrolytes. The ability to employ a wide
82 range of different nitrate salts in the spray drying approach makes it possible to synthesize
83 electrolytes with a wide range of different composition. We first show that a conventional Gd-
84 doped ceria (GDC) electrolyte can be easily fabricated and the resulting electrical properties
85 (measured with impedance spectroscopy) are comparable to GDC electrolytes synthesized with
86 other approaches. We then demonstrate that it is easy to introduce multiple dopants into the
87 formulation by preparing an electrolyte co-doped with Gd and Pr. Finally, we investigate the
88 effect of single and double doping on the grain boundary structure, chemistry and electrical
89 conductivity. Analysis of electrical properties shows that the grain boundaries in the co-doped
90 sample are almost 100 times more conducting than the singly doped boundaries. The enhanced
91 conductivity may be the result of strong Pr segregation to the grain boundaries that we observe
92 using aberration corrected scanning transmission electron microscope (STEM) and electron
93 energy-loss spectroscopy (EELS).

94 **2. Experimental**

95 We fabricated doped ceria powders using a spray-drying synthesis technique developed by
96 the authors and described elsewhere [6]. In this technique, an aqueous solution is sprayed as a
97 fine mist into a reaction vessel where it is introduced to a stream of air heated to approximately
98 300 °C. The hot air rapidly dries the solution droplets and initiates the decomposition of the
99 nitrate precursors into oxide. Precursors of 99.998% purity $\text{Ce}(\text{NO}_3)_3 \cdot 6\text{H}_2\text{O}$, $\text{Gd}(\text{NO}_3)_3 \cdot 6\text{H}_2\text{O}$,
100 and $\text{Pr}(\text{NO}_3)_3 \cdot 6\text{H}_2\text{O}$ (Alpha Aesar, Ward Hill, MA) were combined in the appropriate amounts in

101 a 0.1 M aqueous solution to yield powders of nominal composition $\text{Gd}_{0.2}\text{Ce}_{0.8}\text{O}_{2-\delta}$ (GDC) and
102 $\text{Gd}_{0.11}\text{Pr}_{0.04}\text{Ce}_{0.85}\text{O}_{2-\delta}$ (GPDC). The powders were extracted from the reaction vessel using
103 methanol, allowed to dry under air, calcined at 500 °C for 2 h, crushed in a mortar and pestle,
104 and calcined further at 900 °C for 5 h. The heating rate for both calcinations was 5 °C/min,
105 followed by furnace cooling. These additional heat treatments complete the nitrate
106 decomposition and result in nanoscale oxide powders that are suitable for further ceramic
107 processing. The powder was then pressed into cylindrical pellets 18 mm in diameter and
108 approximately 1 mm thick using a hardened steel die under uniaxial compression (180 MPa) at
109 room temperature. Finally, pellets were sintered in air at 1350 °C for 18 h with a 2.5 °C/min
110 heating rate followed by furnace cooling.

111 The parallel faces of the sintered pellets were polished using 1 μm polishing paper and then
112 coated with Pt ink (Fuel Cell Materials, Columbus, OH). Pt wires were submerged in the ink and
113 the assembly placed in a 100 °C oven for 1 h prior to firing at 1000 °C for 1 h (1 °C/min heating
114 rate, furnace cooling). AC impedance spectroscopy was performed on the pellets under air using
115 a Gamry Reference 3000 potentiostat (Gamry Instruments, Westminister, PA) with an excitation
116 voltage of 50 mV over the frequency range of 0.1 Hz to 1 MHz and the sample temperature was
117 monitored with a K-type thermocouple. Samples were heated in a stepwise manner, and
118 impedance spectra were acquired at each dwell temperature. Impedance data were analyzed with
119 the Gamry EChem Analyst software package. Uncertainties in the measured conductivities and
120 activation energies are determined from uncertainty in fitting the experimental impedance data to
121 an equivalent circuit model.

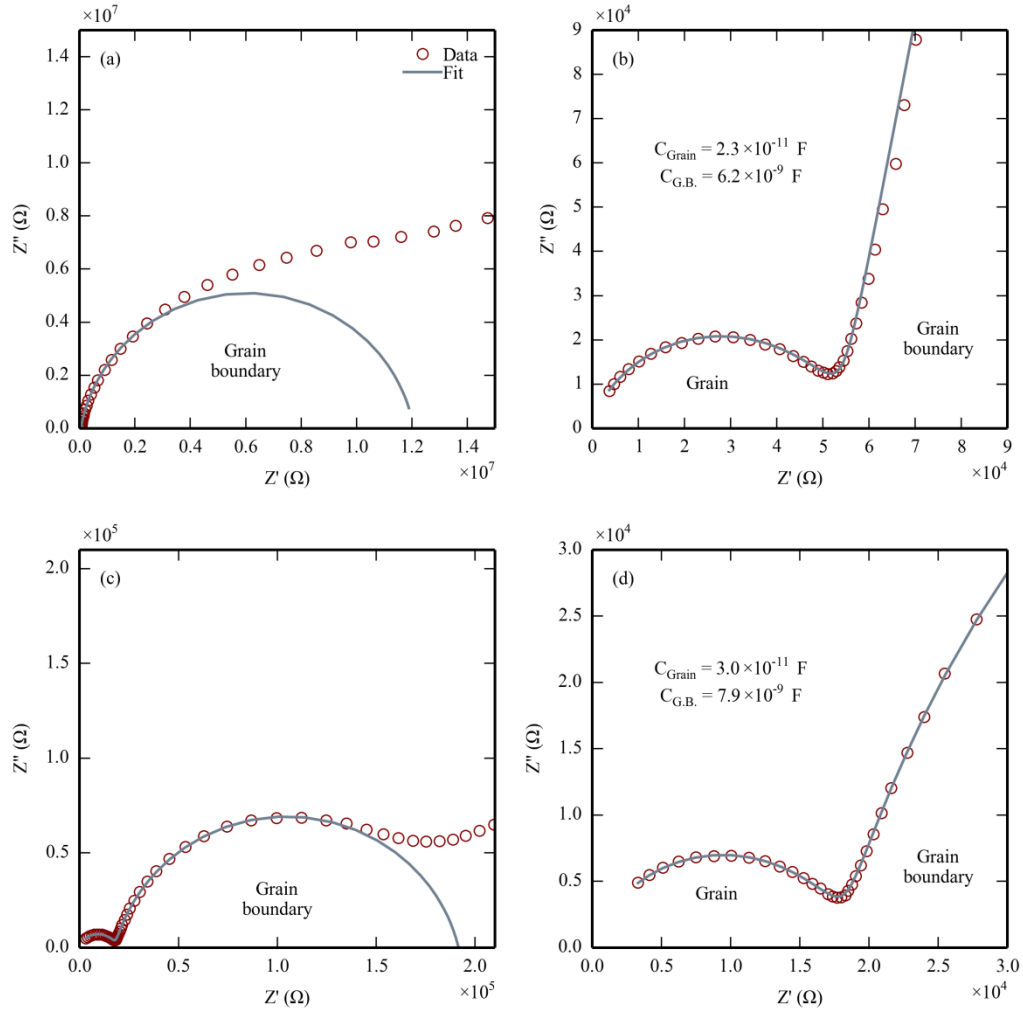
122 TEM was used to characterize grain size, microscale compositional homogeneity, nanoscale
123 structure and chemistry of grain boundaries. Following impedance spectroscopy, a GDC TEM

124 specimen is prepared by cutting a 3 mm diameter disc from the pellet using an ultrasonic disc
125 cutter (Gatan Inc., Pleasanton, CA). The disc was ground to a thickness of approximately 110 μm
126 and then dimpled to approximately 20 μm with a Gatan Dimple Grinder. The dimpled specimen
127 was then ion milled to electron transparency in a Gatan PIPS2 ion mill using 4 keV Ar^+ ions with
128 an incidence angle of 8° on top and bottom for 120 min, followed by 2 keV Ar^+ ions at 4° top
129 and bottom for 40 min. The GPDC specimen was prepared by standard lift-out techniques in a
130 FEI Nova 200 NanoSEM (FEI Co., Hillsboro, OR) equipped with Ga^+ focused ion beam [24].
131 High resolution imaging, energy dispersive x-ray spectroscopy (EDX), and EELS in a STEM
132 were performed using a Phillips CM200 FEG (200 kV), JEOL 4000EX (400 kV), JEOL 2010F
133 (200 kV) and a JEOL ARM200F (200 kV) (JEOL Ltd., Tky, Japan). Microscope data were
134 processed using ES Vision (Emispec Systems Inc., Tempe, AZ), Gatan Digital Micrograph, and
135 ImageJ, and the Pyzo Python integrated development environment (Open source, [25]). The
136 uncertainty in the measured width of the grain boundary composition profiles is the standard
137 deviation from the mean width measured at different positions along the grain boundaries.

138

139 **3. Results and discussion**

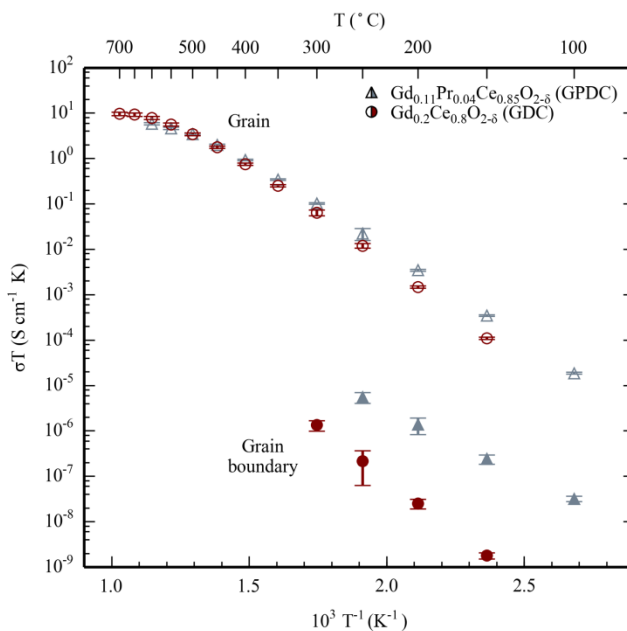
140 **3.1. Electrical properties**



141
142 **Figure 1. Nyquist plots from (a, b) $\text{Gd}_{0.2}\text{Ce}_{0.8}\text{O}_{1.9}$ (GDC) and (c, d) $\text{Gd}_{0.11}\text{Pr}_{0.04}\text{Ce}_{0.85}\text{O}_{2-\delta}$**
143 **(GPDC) acquired at 200 °C. Spectra (b) and (d) show the high frequency portions of**
144 **spectra (a) and (c), as well as the corresponding grain and grain boundary capacitance**
145 **values determined from fit parameters.**

146 Figure 1 displays representative impedance data as Nyquist plots acquired at 200 °C from
147 pellets fabricated from spray dried GDC and GPDC powders. Both spectra exhibit two arcs
148 corresponding to the grain interior and grain boundary polarizations. An arc corresponding to the

149 electrode polarization was also visible in the GPDC spectrum; however, it was not included in
 150 the curve fitting procedure described below. Nyquist plots were interpreted by fitting to an
 151 equivalent circuit model comprised of a series combination of two parallel RQ circuits (grain and
 152 grain boundary polarization), where Q represents the constant phase element (used when
 153 modeling imperfect capacitors) [29]. At higher measurement temperatures, the Nyquist plot
 154 shifted to lower impedance and the grain-interior arc became inaccessible due to the 1 MHz
 155 upper frequency limit of the potentiostat, as well as the reduced time constant of the polarization
 156 relaxation at elevated temperatures [7]. When the grain-interior arc was not visible, the grain-
 157 interior resistance was determined from fits of the grain-boundary arc only. The parallel RQ
 158 component corresponding to the grain in the equivalent circuit in these cases was replaced with a
 159 single resistor whose value was assumed to be that of the grain-interior resistance. The
 160 capacitance values given for the grain and grain boundary arcs are consistent with previously
 161 reported values for Sm-doped ceria grain and grain boundary capacitances [26].



162

163 **Figure 2. Arrhenius plots of electrical conductivity for $\text{Gd}_{0.11}\text{Pr}_{0.4}\text{Ce}_{0.85}\text{O}_{2-\delta}$ (GPDC) and**
 164 **$\text{Gd}_{0.2}\text{Ce}_{0.8}\text{O}_{2-\delta}$ (GDC).**

165 Figure 2 shows Arrhenius plots of the grain interior and grain boundary electrical conductivities
 166 for GPDC and GDC. The grain-interior conductivity, σ_{∞} , was calculated using

$$\sigma_{\infty} = \frac{1}{R_{\infty}} \times \left(\frac{t}{A} \right) \quad (1)$$

167 where R_{∞} , t , and A denote the grain interior resistance, electrode separation and electrode area,
 168 respectively [8]. The grain boundary conductivity, σ_{gb} , was calculated from

$$\sigma_{gb} = \frac{\tau_{\infty}}{\tau_{gb}} \times \sigma_{\infty} \quad (2)$$

169 using the time constants of the grain interior and grain boundary polarizations (τ_{∞} and τ_{gb} ,
 170 respectively), as well as the grain-interior conductivity [29]. Because a constant phase element
 171 was used instead of capacitors in the equivalent circuit model, time constants (i.e. $\tau = RC$) were
 172 determined from capacitances calculated from

$$C = (R^{(1-\alpha)}Y)^{1/\alpha} \quad (3)$$

173
 174 As shown by others, the GDC conductivities are assumed to be ionic under non-reducing
 175 conditions (e.g. [27]). The measured grain conductivity for the GDC electrolyte prepared here is
 176 in good agreement with those published by Avila-Paredes et al. [8], Zhang et al. [9] and Jasper et
 177 al. [28]. The grain interior conductivity in GDC measured at 300 °C is $(1.5 \pm 0.05) \cdot 10^{-4} \text{ S}\cdot\text{cm}^{-1}$,
 178 agrees with the value measured by Avila-Paredes et al. of approximately $1 \cdot 10^{-4} \text{ S}\cdot\text{cm}^{-1}$ at
 179 300 °C [8]. At 200 °C we find the specific grain boundary conductivity to be $(7 \pm 2) \cdot 10^{-11}$
 180 $\text{S}\cdot\text{cm}^{-1}$, approximately 10 times less than that of Avila-Paredes et al. In high-purity materials,
 181 such as those used here, the grain-boundary conductivity will be affected by space-charge effects

182 as well as the structural and compositional character of grain boundaries. Figure 2 shows that the
183 grain-boundary conductivity at 200 °C is 5×10^4 times lower than the grain-interior
184 conductivity in GDC, clearly demonstrating the deleterious effect of grain boundaries on ionic
185 conductivity especially at low temperatures. This also illustrates the need to develop a
186 fundamental understanding of the relationship between charge transport, grain-boundary
187 structure and composition. Such an understanding may allow grain-boundary tailoring to be
188 accomplished, leading to substantial improvements in ionic conductivity in polycrystalline
189 electrolytes.

190 In GPDC the grain-interior conductivity at 300 °C was measured to be $(2.1 \pm 0.05) \cdot 10^{-4}$
191 $\text{S}\cdot\text{cm}^{-1}$, approximately 40 % higher than that of GDC. The higher grain-interior conductivity of
192 this material compared to the GDC sample is in agreement with theoretical results from
193 Dholabhai et al. [3], and reasonable considering that $\text{Gd}_{0.1}\text{Ce}_{0.9}\text{O}_{1.95}$ was shown experimentally to
194 yield higher grain-interior ionic conductivity than $\text{Gd}_{0.2}\text{Ce}_{0.8}\text{O}_{1.9}$ [8]. Furthermore, the
195 incorporation of Pr has been demonstrated to increase both ionic conductivity and p-type
196 electronic conductivity in $\text{Gd}_{0.2-x}\text{Pr}_x\text{Ce}_{0.8}\text{O}_{2-\delta}$ for $x < 0.03$ [4,5]. While our observations agree
197 with these findings qualitatively, the exact origin of increased grain interior conductivity due to
198 Pr doping remains ambiguous at this time.

199 The effect of grain boundaries in the doubly-doped material is much less detrimental than in
200 the GDC. Indeed if we compare the grain boundary conductivities of the two materials at 200 °C
201 we find that the GPDC specific grain boundary conductivity is $(3 \pm 1) \cdot 10^{-9} \text{S}\cdot\text{cm}^{-1}$,
202 approximately 50 times that of GDC ($(6 \pm 1) \cdot 10^{-11} \text{S}\cdot\text{cm}^{-1}$). This result suggests a significant
203 effect on the grain-boundary electrical properties due to the addition of Pr, and is particularly
204 surprising considering that Avila-Paredes and coworkers [8] found that the grain boundary

205 conductivity in $\text{Gd}_{0.1}\text{Ce}_{0.9}\text{O}_{2-\delta}$ — the approximate Gd concentration of our GPDC, was
 206 approximately five times lower than that of $\text{Gd}_{0.2}\text{Ce}_{0.8}\text{O}_{2-\delta}$. One possible explanation for the
 207 higher grain-boundary conductivity in the GPDC is the effect of Pr segregation to grain
 208 boundaries discussed in the next section.

209 Activation energies, E_a , for the grain-interior and grain-boundary conductivities were
 210 calculated from Arrhenius slopes using equation (4)

$$\sigma T = \sigma_0 e^{\frac{-E_a}{kT}} \quad (4)$$

211
 212 Because the associations between oxygen vacancies and cations become insignificant at higher
 213 temperatures [8], there is a distinct change in the Arrhenius slope at approximately 450 °C. Thus,
 214 grain-interior activation energies were determined for $T < 450$ °C and $T \geq 450$ °C. (Grain-
 215 boundary activation energies were determined only from measurements made below 300 °C.)
 216 Results of these calculations are tabulated in Table 1.

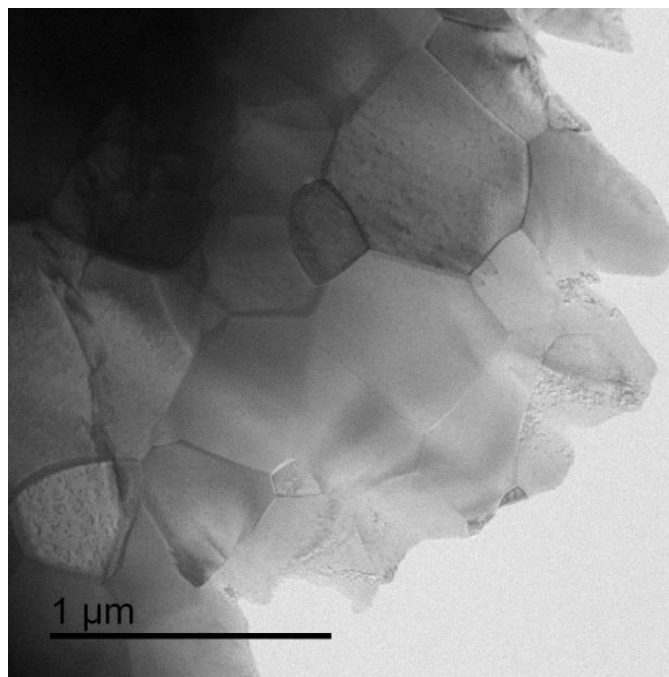
217 **Table 1. Summary of data for all samples**

Sample Nominal composition	Average grain size (μm)	Grain interior E_a T < 450 °C (eV)	Grain interior E_a T \geq 450 °C (eV)	Grain Boundary E_a (eV)
$\text{Gd}_{0.2}\text{Ce}_{0.8}\text{O}_{1.9}$ (GDC)	0.75 \pm 0.31	0.87 ± 0.02	0.42 ± 0.04	0.92 ± 0.20
$\text{Gd}_{0.11}\text{Pr}_{0.04}\text{Ce}_{0.85}\text{O}_{2-\delta}$ (GPDC)	0.45 \pm 0.18	0.78 ± 0.01	0.39 ± 0.04	0.58 ± 0.10

218 For GDC, the activation energies for grain-interior and grain boundary ionic conductivities
 219 are comparable with previous works [5,8]. The activation energies for GPDC with $T < 450$ °C
 220 are lower than for GDC, which is consistent with our observation of higher conductivity in the
 221 doubly-doped material. This trend also agrees with the report of Lubke et al; however, the
 222 absolute values vary somewhat, likely due to differences in the Gd and Pr doping levels.

223 Interestingly, the GPDC grain boundary activation energy is significantly lower than that of the
224 grain interior. This may stem from electronic conduction induced in the boundary region as a
225 result of significant Pr segregation (see below) [36].

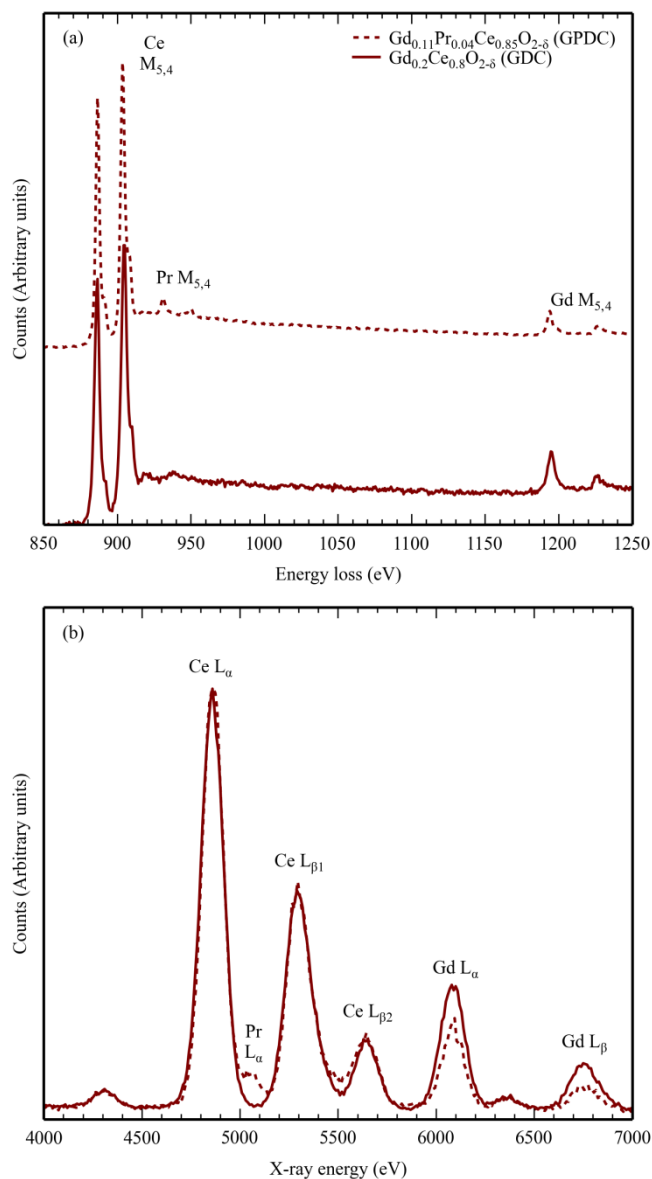
226 3.2. Nanoscale structure and chemistry



227

228 **Figure 3. Low magnification bright field TEM micrograph of sintered GPDC.**

229 TEM imaging revealed that sintered ceramics have a dense single-phase polycrystalline
230 microstructure (fig.3). X-ray diffraction and analysis of electron diffractograms from GDC
231 (Figure 8a inset) and GPDC (fig. 5a inset) confirmed that both materials have a fluorite structure.
232 Scanning electron micrographs and low magnification images of the sintered samples were used
233 to estimate the average grain size of the ceramics (e.g. fig. 3). There was a decrease in the grain
234 size with increasing total dopant concentration which is consistent with previous observations of
235 sintered undoped and Gd-doped ceria [14].



236

237 **Figure 4. (a) electron energy-loss spectra and (b) energy dispersive x-ray spectra from**

238

GPDC and GDC

239 EELS and EDX spectra were collected from GDC and GPDC grains to investigate the

240 distribution of dopant cations following sintering. Figure 4a compares typical energy-loss spectra

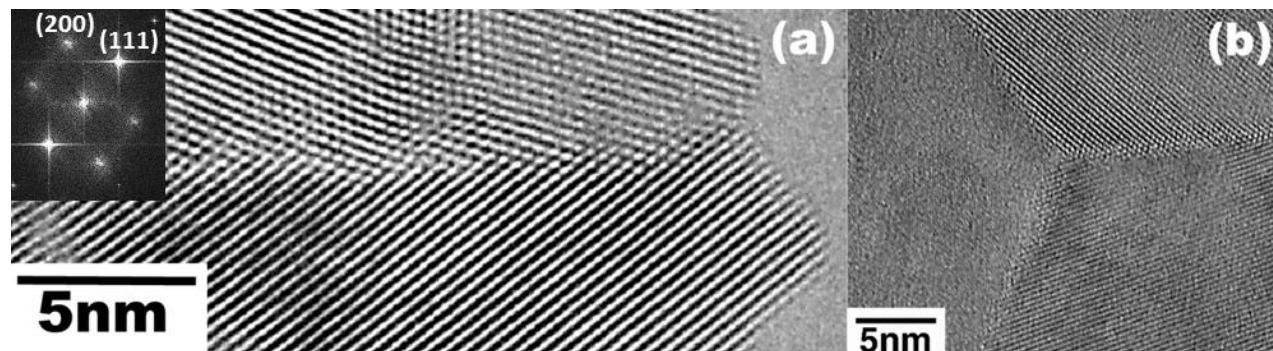
241 from GPDC and GDC. The Gd $M_{5,4}$ *white lines* confirmed the presence of Gd in each grain of

242 both samples, while the Pr $M_{5,4}$ edge confirmed the presence of Pr in all grains of the co-doped

243 GPDC. Figure 4b compares typical GPDC and GDC EDX spectra (normalized to the Ce L_{α} line

244 in GPDC). The Pr L_{α} line which is visible in the GPDC spectra was used to indicate the presence
245 of Pr. EELS and EDX showed that Gd and Pr were present in all grains analyzed in the GPDC
246 confirming the effectiveness of the spray drying approach to produce polycrystalline tertiary and
247 quaternary rare earth oxides.

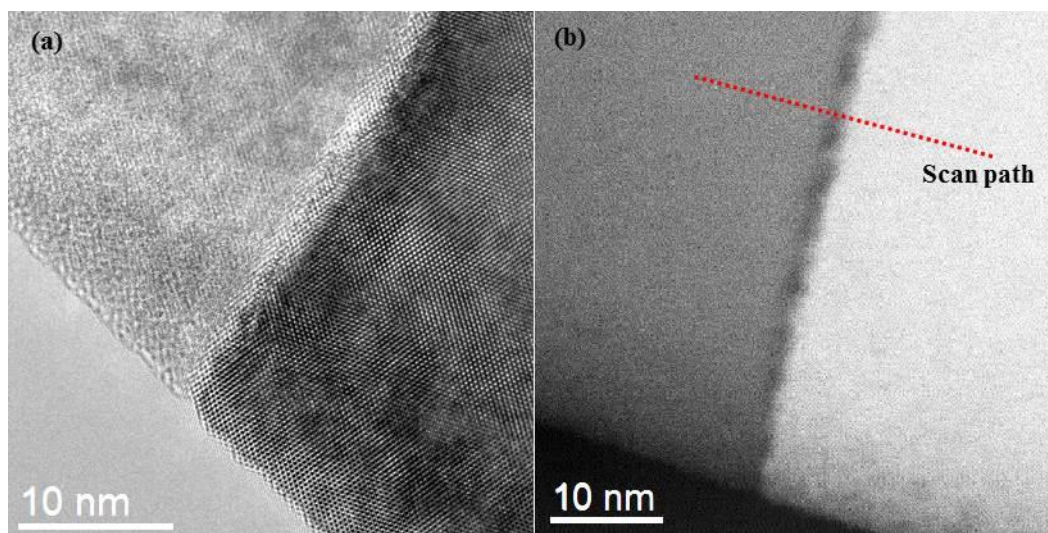
248 **The true composition of the materials investigated was assumed to be approximately that of**
249 **the nominal composition. It is possible that the nitrate-hydrate precursor compounds were**
250 **somewhat dehydrated at the time of synthesis, which could cause discrepancy between the**
251 **nominal and true composition. However, because the melting points of the Gd- and Ce-nitrate-**
252 **hexahydrates are approximately the same (91 °C and 96 °C, respectively) it is likely that both**
253 **were equally dehydrated at room temperature keeping the cation ratio within 0.5% of its nominal**
254 **value.**



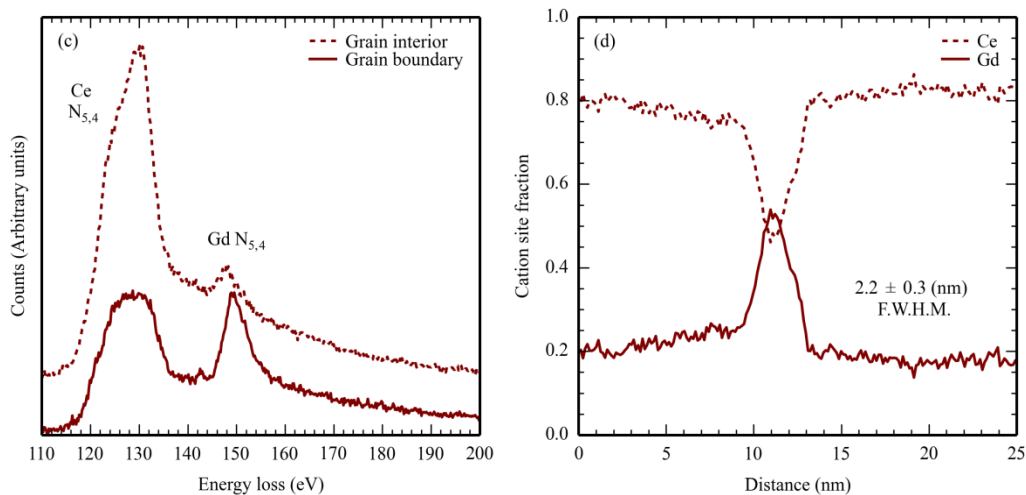
255
256 **Figure 5. (a) BF TEM micrograph of a typical GPDC grain boundary with $[0\bar{1}1]$ zone axis**
257 **diffractogram inset, and (b) triple grain junction in the sintered GPDC.**

258 As the presence of an amorphous intergranular phase and/or dopant segregation to grain
259 interface regions are expected to affect grain-boundary transport properties, high-resolution
260 imaging was used to investigate the structure of grain boundaries following sintering. All grain
261 interfaces, like those shown in Figure 5 for GPDC, appeared to be structurally abrupt and free of
262 significant amorphous intergranular phases, an observation consistent with the work of previous

263 researchers [28,29]. Again we find that the spray drying technique produces material with
264 microstructures comparable to those produced by other preparation methods.



265

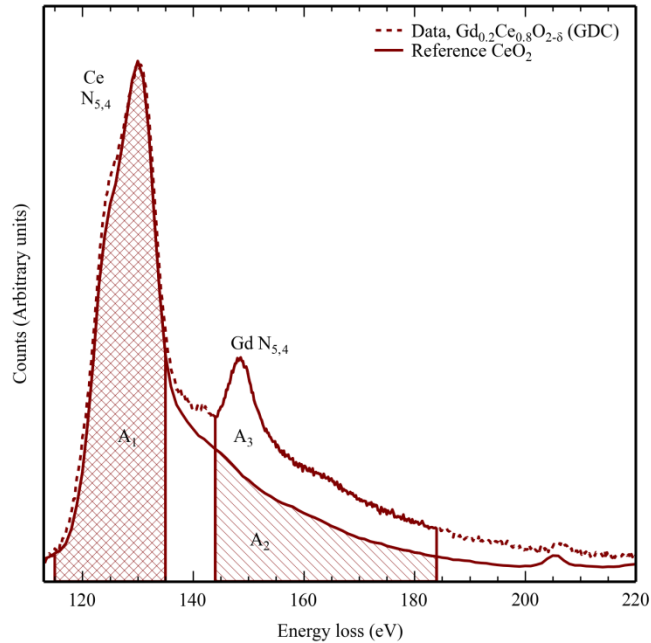


266

267 **Figure 6. (a) BF TEM and (b) ADF STEM micrographs of a typical grain boundary in**
268 **GDC. (c) Electron-energy loss spectra from GDC acquired at the grain boundary core and**
269 **grain interior depicted in (b). (d) Ce and Gd N_{5,4} edge profiles corresponding to the scan**
270 **path shown in (b). (STEM probe size was ≈ 0.2 nm)**

271 To investigate variations in cation concentrations (Ce, Pr, and Gd) at the boundaries (which
272 are not readily apparent via imaging), STEM EELS was performed. Figure 6a shows a bright

273 field (BF) TEM micrograph of a grain boundary which is slightly tilted, but clean (i.e. free of
274 amorphous material). Diffraction contrast variation is visible in the two adjacent grains,
275 indicating that the right grain is in a stronger electron diffracting condition than the left. Figure
276 6b shows an annular dark field (ADF) STEM image of the same grain boundary; the dotted line
277 depicts the scan path of the STEM EELS linescan in (d). There is visible contrast variation
278 caused by misorientation between adjacent grains, as well as dark contrast at the grain boundary
279 core. The dark contrast visible at this grain boundary core is believed to be the result of the more
280 open interfacial atomic structure scattering fewer electrons to the annular detector, thus resulting
281 in a less intense signal at the grain-boundary core relative to the adjacent grains. Figure 6c
282 compares energy-loss spectra acquired from the grain interior and the grain-boundary core.
283 There is a marked increase in the Gd $N_{5,4}$: Ce $N_{5,4}$ edge integrated intensity ratio at the grain
284 boundary core indicating considerable enhancement of the Gd concentration at the grain
285 boundary. The spectra also show that the Ce edge is much more rounded at the grain boundary
286 indicating that a significant change in local Ce bonding has taken place in the grain-boundary
287 core.



288
 289 **Figure 7. Background-subtracted experimental GDC and reference CeO₂ ([30]) energy loss**
 290 **spectra with highlighted integration windows used for peak overlap correction. (The CeO₂**
 291 **spectrum is normalized to the GDC Gd N_{5,4} edge maxima.)**

292 Figure 7 shows the N_{5,4} region of a typical experimental GDC energy-loss spectrum, plotted
 293 with a CeO₂ reference spectrum (normalized to the GDC Gd N_{5,4} maxima) and highlighted
 294 integration windows used for overlap correction and quantification. Because the tail of the Ce-
 295 N_{5,4} edge overlaps the Gd N_{5,4} edge onset in the energy loss range 144 eV – 184 eV (see Fig. 7
 296 windows A₂ and A₃), quantification of GDC energy-loss spectra like those in Figure 6c required a
 297 correction procedure. The ratio of integrated intensity in window A₁ (115 eV to 135 eV) to that in
 298 A₂ was assumed constant so that the contribution of the Ce N_{5,4} edge tail to the in energy loss
 299 range 144 eV to 184 eV (i.e. A₂) could be subtracted, leaving only intensity from the Gd N_{5,4} (i.e.
 300 A₃). In other words, the goal of the quantification process was to isolate the Gd N_{5,4} integrated

301 intensity (A_3) from the combined Ce + Gd N_{5,4} signal ($A_2 + A_3$) in the 144 eV to 184 eV energy
 302 loss window.

303 It should be noted that a 40 eV energy loss range was selected for the Gd integration window
 304 is a compromise to maximize the signal strength and minimize extrapolation errors [31]. The
 305 intensity in the Gd N_{5,4} signal, I_{Gd} , in the energy loss spectra from GDC can be expressed as

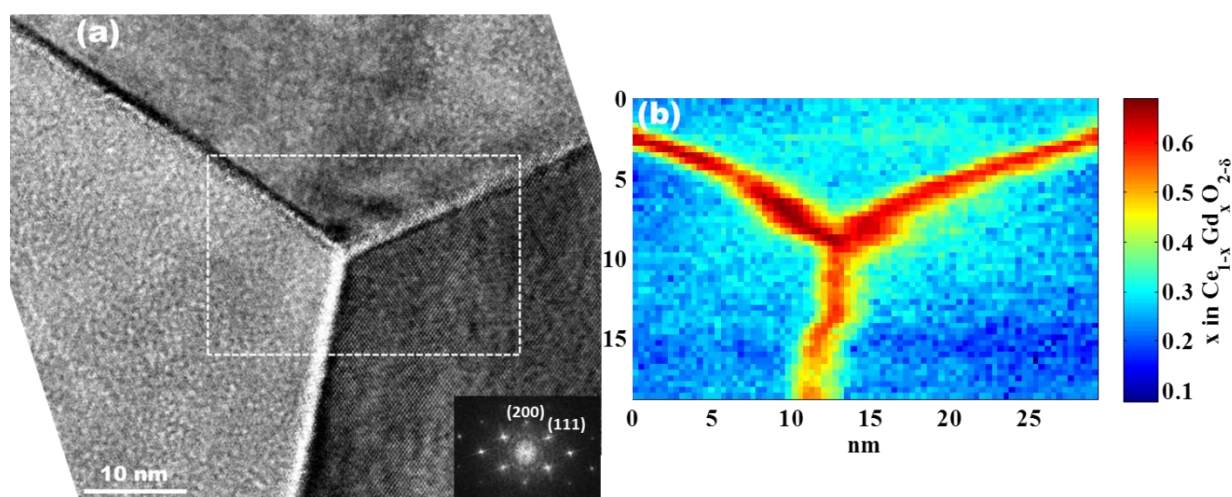
$$I_{Gd} = A_3 = (A_2 + A_3)^{GDC\ exp.} - A_1^{GDC\ exp.} \left(\frac{A_2}{A_1} \right)^{CeO_2\ Ref.} \quad (5)$$

306 The quantity $(A_2/A_1)^{CeO_2\ Ref.}$ is the integrated intensity ratio of the Ce N_{5,4} tail to the Ce N_{5,4}
 307 edge determined from the CeO₂ reference spectrum. This quantity was multiplied by the
 308 measured Ce N_{5,4} edge intensity, $A_1^{GDC\ exp.}$, to approximate the Ce tail contribution ($A_2^{GDC\ exp.}$)
 309 to the total signal in the Gd-N_{4,5} energy loss window, $(A_2 + A_3)^{GDC\ exp.}$. Knowledge of the Gd-
 310 N_{5,4} signal, I_{Gd} , enabled estimation of the $[Gd]/[Ce]$ concentration ratio using

$$\frac{[Ce]}{[Gd]} = \frac{I_{Ce}}{I_{Gd}} * \frac{\sigma_{Gd}}{\sigma_{Ce}} \quad (6)$$

311 where I_{Ce} and I_{Gd} are the signals in the energy loss spectrum integrated over 115 eV to 135 eV
 312 and 144 eV to 184 eV, respectively, and σ_{Ce} and σ_{Gd} are the relevant inelastic scattering cross
 313 sections [32]. To estimate compositional variations at grain boundaries, we assumed both
 314 nominal cation composition at grain interiors (i.e. $([Ce]/[Gd])_{\infty} = 4$), as well as constancy of
 315 the cross-section ratio (i.e. $\sigma_{Gd}/\sigma_{Ce} = k$). This so-called k factor was determined to be $0.32 \pm$
 316 0.03 using $I_{Ce}:I_{Gd}$ ratios acquired at grain interiors. The concentrations were determined by using
 317 equation (6) and assuming that the cation concentrations sum to 1 (or 100 for percentages). The
 318 typical fractional error associated with concentrations was 0.05 to 0.1 determined from
 319 uncertainty in the calculated k-factor.

320 Figure 6d shows the result of this k-factor analysis for a linescan along the highlighted scan
321 path across the grain boundary in Figure 6b. The composition was found to vary significantly
322 along the scan path, from approximately $\text{Gd}_{0.2}\text{Ce}_{0.8}\text{O}_{1.9}$ in the grain interiors to approximately
323 $\text{Gd}_{0.55}\text{Ce}_{0.45}\text{O}_{2-\delta}$ at the grain-boundary core. The width of this Gd enhancement zone, measured
324 from the full-width half-maxima of the concentration profile, was estimated to be (2.2 ± 0.3) nm.

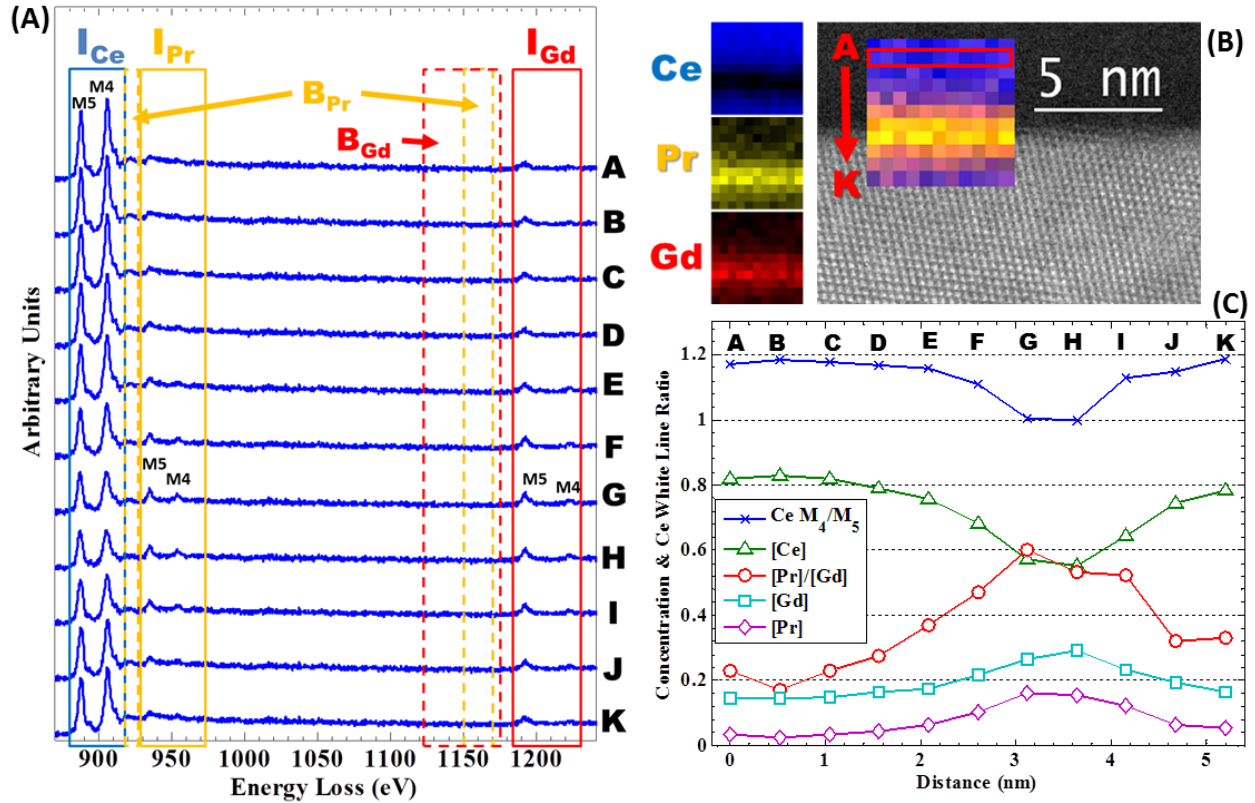


325
326 **Figure 8. (a) BF TEM micrograph of a triple grain junction in GDC with $[0\bar{1}1]$ zone axis**
327 **diffraction inset on the corresponding grain. (b) STEM EELS 2D elemental map**
328 **indicating the distribution of Gd in the region of the junction. (STEM probe size was \approx**
329 **0.2nm.)**

330 Triple grain junction regions in GDC were also investigated using STEM EELS 2D
331 elemental mapping. This made it possible to visualize the spatial extent of cation concentration
332 fluctuations along grain boundaries, and in the vicinity of the triple-grain junction. Figure 8a
333 shows a BF TEM micrograph of one such junction in GDC with the corresponding elemental
334 map provided in Figure 8b. The slight distortion in the grain boundary shape visible in the map is
335 due to specimen drift during the STEM EELS spectrum image acquisition. The average fraction
336 of cation sites occupied by Gd in the grain boundary core is approximately 0.55, similar to the

337 grain boundary line scan in Figure 6b. Though, in some regions there does appear to be
338 considerable non-uniformity in the Gd distribution, with the cation site occupancy fraction of Gd
339 ranging from 0.4 to 0.7. The estimated average grain boundary core cation site occupancy
340 fraction of Gd was 0.62 ± 0.03 , which is comparable with previous work of Lei et al. who
341 measured a grain boundary composition of $\text{Gd}_{0.41 \pm 0.04}\text{Ce}_{0.59 \pm 0.04}\text{O}_{1.24 \pm 0.17}$ in a nominally
342 $\text{Gd}_{0.2}\text{Ce}_{0.8}\text{O}_{2-\delta}$ electrolyte [33]. These authors also measured the width of the Gd-segregation
343 region (i.e. the chemical grain boundary) to be approximately 2 nm to 2.5 nm, which is
344 consistent with the 2.2 ± 0.3 nm chemical grain boundary width observed in this work. Lee et al.
345 also reported Gd enhancement extending approximately 1.5 nm to 2 nm from grain boundary
346 cores in $\text{Gd}_{0.3}\text{Ce}_{0.7}\text{O}_{2-\delta}$ thin films using STEM EDS [34].

347 As discussed above, we measured the specific grain-boundary conductivity of the GPDC
348 ($\text{Gd}_{0.11}\text{Pr}_{0.04}\text{Ce}_{0.85}\text{O}_{2-\delta}$) to be approximately 50 times that of the GDC ($\text{Gd}_{0.2}\text{Ce}_{0.8}\text{O}_{2-\delta}$) at 200 °C.
349 This result was particularly interesting considering the work of Avila-Paredes and Kim, who,
350 when varying the Gd cation fraction (x) in $\text{Gd}_x\text{Ce}_{(1-x)}\text{O}_{2-\delta}$ ($0.01 < x < 0.2$), found the specific
351 grain-boundary conductivity of x = 0.2 sample to be approximately five times greater than that of
352 the x = 0.1 sample at approximately 200 °C. In light of this result, we concluded that the higher
353 specific grain-boundary conductivity in our GPDC was the result of Pr doping, as doping with
354 0.2 Gd cation fraction should have resulted in higher grain boundary conductivity than 0.11 Gd
355 cation fraction.



356

357 **Figure 9. (a) Background-subtracted energy loss spectra acquired from $\text{Gd}_{0.11}\text{Pr}_{0.04}\text{Ce}_{0.85}\text{O}_{2-\delta}$**

358 **showing variations in the Ce, Pr and Gd M_{4,5} edges across the grain boundary in (b). (b)**

359 **Aberration-corrected STEM image of a grain boundary with inset color map illustrating**

360 **the cation distribution in the interfacial region; constituent color maps are provided. (c)**

361 **Profiles of estimated cation fraction and the Ce M₄/M₅ white line ratio—an indicator of the**

362 **Ce oxidation state. (STEM probe size was ≈ 0.1 nm.)**

363

To explore effects of Pr doping on grain boundaries, variations in constituent cation fractions

364

and Ce oxidation state were studied with EELS using an aberration corrected TEM/STEM

365

operating at 200 kV. Figure 9a illustrates the effect of the grain boundary on the M_{5,4} edges of

366

Ce, Pr and Gd. Each background-subtracted spectrum is labeled A \rightarrow K and represents the sum

367

of all spectra in each row of the inset spectrum image in Figure 9b, also labeled A \rightarrow K and

368

highlighted with a rectangular box. The integration (I_{Ce} , I_{Pr} and I_{Gd}) and background fitting (B_{Pr}

369 and B_{Gd}) windows used for spectrum quantification are highlighted with solid and dashed boxes,
370 respectively in figure 9a. Though omitted for clarity, a 45 eV-wide background fitting window
371 positioned 5 eV to the left of the Ce $M_{5,4}$ integration window was used for quantification.
372 Because of the close proximity of the Pr and Ce edge onsets, a two window background fitting
373 procedure was adopted to extract the Pr signal with one narrow window just in front of the Pr
374 $M_{5,4}$ edge and a second just before the Gd $M_{5,4}$ edge. Figure 9b shows an ADF STEM image of
375 a grain boundary in GPDC with an inset energy-loss spectrum image. The spectrum image is
376 false colored by overlaying the color maps (left of STEM image) derived from integrating the
377 $M_{5,4}$ signal for each cation at every pixel. Figure 9c displays variations in the estimated cation
378 concentration, the relative dopant concentration, as well as the Ce M_4/M_5 white line ratio, which
379 is an indication of the oxidation state of the Ce ion [35]. The data points are separated by
380 approximately 5.2 Å and labeled $A \rightarrow K$ to indicate the row in the spectrum image from which
381 they were derived. From inspection of these figures, position H is taken to be the approximate
382 position of the grain boundary core.

383 Figure 9a shows significant variation in the cation concentration and the Ce oxidation state
384 with position in the grain boundary region. Distinct increases in the $I_{Pr}:I_{Ce}$ and $I_{Gd}:I_{Ce}$ signal
385 intensity ratios are clearly visible, indicating an enhancement of the Pr and Gd concentrations
386 relative to Ce. Like the GDC, this enhancement is attributed to dopant segregation during
387 sintering of the bulk ceramic disc. Also visible is a decrease in the Ce M_4/M_5 white line ratio
388 from $M_4/M_5 \approx 1.2$ at grain interiors to $M_4/M_5 \approx 1.0$ at the boundary core. This change is
389 characteristic of the reduction of Ce^{4+} to $Ce^{(4-y)+}$ ($0 \leq y \leq 1$), and suggests the absence of bonded
390 oxygen ions [35]. This white-line ratio reaches a minimum at the grain boundary core,

391 presumably due to the oxygen non-stoichiometry associated with the highly defective core
392 structure of this particular grain boundary.

393 The dopant segregation profiles are approximately (1.8 ± 0.3) nm wide, a figure similar to
394 that of our GDC. Ce, Pr and Gd cation fractions were estimated using a k-factor analysis routine
395 similar to that described for GDC above, and found to be 0.55, 0.16 and 0.29 at the boundary
396 core, respectively. Interestingly, the relative dopant concentration ratio ($[\text{Pr}]:[\text{Gd}]$) was found to
397 vary between approximately 0.28 at grain interiors and 0.55 at the boundary core showing that a
398 greater fraction of Pr segregates to the boundary compared to Gd. The FWHM peak width of the
399 white line ratio profile is approximately 0.8 nm, consistent with the structural width of grain
400 boundaries visible in high resolution images herein. This indicates that the reduced ceria is
401 associated with the grain boundary core.

402 Enhancements in both ionic and electronic conductivity may play a role in the enhanced
403 grain-interior and grain boundary conductivities of GPDC sample relative to the GDC sample,
404 though the active charge transport mechanisms have not been fully identified. Previous
405 theoretical work based on DFT calculations and Monte Carlo simulations predicted increased
406 grain-interior ionic conductivity in Gd/Pr doubly-doped ceria, with enhancements dependent on
407 relative dopant concentrations (i.e. $[\text{Pr}]:[\text{Gd}]$) [3]. Here, greater grain-boundary conductivity of
408 the GPDC sample relative to the GDC sample correlates with a high Pr segregation to the
409 boundary. A plausible explanation for the greater GPDC grain boundary conductivity is an
410 increase in ionic conductivity due to a reduction in the oxygen vacancy migration energy
411 associated with Pr segregation to grain interfaces [3]. Moreover, such high Pr doping levels
412 would very likely facilitate small polaron hopping [4,36] in the vicinity of grain boundaries,
413 giving rise to considerable electronic current through the boundary. Such a contribution from an

414 electronic current is reasonable when the very significant reduction in observed migration
415 activation energy of the grain boundary is also considered.

416

417 4. Conclusions

418 $\text{Gd}_{0.2}\text{Ce}_{0.8}\text{O}_{2-\delta}$ (GDC) and $\text{Gd}_{0.11}\text{Pr}_{0.04}\text{Ce}_{0.85}\text{O}_{2-\delta}$ (GPDC) powders were successfully
419 synthesized with spray drying, and used to fabricate sintered pellets for bulk electrical
420 characterization by AC impedance spectroscopy performed between 150 °C and 700 °C.
421 Following electrical characterization, specimens were analyzed via scanning transmission
422 electron microscopy (STEM) using high resolution imaging, energy dispersive x-ray
423 spectroscopy (EDX) and electron-energy loss spectroscopy (EELS) in a number of scanning
424 TEMs. Electrical conductivity in GDC was interpreted as ionic conductivity and was in
425 reasonable agreement with previous reports. The grain interior and grain boundary conductivities
426 of the GPDC were higher than GDC by up to 1 and 2.5 orders of magnitude depending on the
427 measurement temperature. Interestingly, the GPDC grain boundary migration activation energy
428 was found to be (0.58 ± 0.1) eV, considerably lower than that of the grain interior which was
429 measured to be (0.92 ± 0.2) eV.

430 TEM analysis indicated that GDC microstructures were consistent with those in the
431 literature. EDX and EELS confirmed the presence of dopants throughout grains in both
432 materials, thus highlighting the efficacy of the spray drying approach to produce sintered pellets
433 with uniform grain-interior doping. Grain boundaries were free of glassy intergranular phases,
434 and significant dopant concentration enhancement was observed. The grain boundary core
435 composition was estimated from EELS to be $\text{Gd}_{0.62}\text{Ce}_{0.38}\text{O}_{2-\delta}$, and $\text{Gd}_{0.29}\text{Pr}_{0.16}\text{Ce}_{0.55}\text{O}_{2-\delta}$ in GDC
436 and GPDC, respectively. Such a large enhancement in Pr concentration at the grain boundary,
437 along with the significant reduction in migration activation energy suggested possible
438 enhancement in ionic conductivity and the formation of an electronic conduction pathway along
439 grain boundaries. In GPDC, the relative dopant concentration ($[\text{Pr}]:[\text{Gd}]$) varied as well in the

440 grain boundary region. Lastly, the oxidation state of the Ce host cation was found to decrease in
441 the grain boundary core, likely indicating the absence of oxygen due to disorder at the grain
442 interface.

443 **5. Acknowledgements**

444 The authors wish to thank the Fulton Undergraduate Research Initiative at Arizona State
445 University, the National Institute of Standards and Technology's Summer Undergraduate
446 Research Fellowship, Arizona State University's Doctoral Enrichment Fellowship, and the
447 National Science Foundation's Graduate Research Fellowship Program for their gracious support
448 without which this work would not have been possible. We also gratefully acknowledge the staff
449 that assisted this work, as well as the use of facilities in the LeRoy Eyring Center for Solid State
450 Science and the John M. Cowley Center for High Resolution Electron Microscopy at Arizona
451 State University. This material is based upon work supported by the National Science
452 Foundation Graduate Research Fellowship Program under Grant No. DGE-1311230, and NSF
453 DMR-1308085.

454 **6. Disclaimer**

455 Any opinions, findings, and conclusions or recommendations expressed in this material are
456 those of the authors and do not necessarily reflect the views of the National Science Foundation.

457 The full description of the procedures used in this manuscript includes identification of
458 certain commercial products and their suppliers. The inclusion of such information should in no
459 way be construed as indicating that such products or suppliers are endorsed by NIST or are
460 recommended by NIST or that they are necessarily the best materials, instruments, software or
461 suppliers for the purposes described.

References

- [1] Omar, S., Wachsman, E. D., Nino, J. C. Higher conductivity Sm³⁺ and Nd³⁺ co-doped ceria-based electrolyte materials. *Solid State Ionics* **178** 1890-1897 (2008).
- [2] Kharton, V.V., Viskup, A.P., Figueiredo, F.M., Naumovich, E.N., Shaulo, A.L., Marques, F.M.B. Electrochemical properties of Pr-doped Ce(Gd)O_{2-δ}. *Materials Letters* **53** 160-164 (2002).
- [3] Dholabhai, P.P., Adams, J.B., Crozier, P.A., Sharma, R. In search of enhanced electrolyte materials: a case study of doubly doped ceria, *Journal of Materials Chemistry* **21** 18991 (2011).
- [4] Bishop, S. R., Stefanik, T. S., Tuller, H. L. Electrical conductivity and defect equilibria of Pr_{0.1}Ce_{0.9}O_{2-δ}. *Physical Chemistry Chemical Physics* **13** 10165-10173 (2011).
- [5] Lübke, S., Wiemhöfer, H.-D. Electronic conductivity of Gd-doped ceria with additional Pr-doping. *Solid State Ionics* **117** 229-243 (1999).
- [6] Sharma, V., Eberhardt, K. M., Sharma, R., Adams, J. B. & Crozier, P. A. A spray drying system for synthesis of rare-earth doped cerium oxide nanoparticles. *Chemical Physics Letters* **495** 280-286 (2010).
- [7] Zhan, Z., Wen, T.-L., Tu, H., Lu, Z.-Y. AC Impedance Investigation of Samarium-Doped Ceria. *Journal of the Electrochemical Society* **148** A427-A432 (2001).
- [8] Avila-Paredes, H.-J., Choi, K., Chen, C.-T., Kim, S. Dopant-concentration dependence of grain-boundary conductivity in ceria: A space-charge analysis. *Journal of Materials Chemistry* **19** 4837-4842 (2009).
- [9] Zhang, T. S., Ma, J., Cheng, H., Chan, S. H. Ionic conductivity of high-purity Gd-doped ceria solutions. *Materials Research Bulletin* **41** 563-568 (2006).

-
- [10] Guo, X., Maier, J. Grain Boundary Blocking Effect in Zirconia: A Schottky Barrier Analysis. *Journal of the Electrochemical Society* **148** E121-E126 (2001).
- [11] Pikalova, E.Y., Murashkina, A.A., Maragou, V.I., Demin, A.K., Strekalovsky, V.N., Tsiadaras, P.E. CeO₂ based materials doped with lanthanides for applications in intermediate temperature electrochemical devices. *International Journal of Hydrogen Energy* **36** 6175-6183 (2011).
- [12] Avila-Paredes, H.-J., Kim, S. The effect of segregated transition metal ions of the grain boundary resistivity of gadolinium doped ceria: Alteration of the space charge potential. *Solid State Ionics* **177** 3075-3080 (2006).
- [13] Rupp, J.L.M., Gauckler, L.J., Microstructures and electrical conductivity of nanocrystalline ceria-based thin films. *Solid State Ionics* **177** 2513-2518 (2006).
- [14] Rupp, J.L.M., Infortuna, A., Gauckler, L.J. Microstrain and self-limited grain growth in nanocrystalline ceria ceramics. *Acta Materialia* **54** 1721-1730 (2006).
- [15] Huang, H., Gür, T.M., Saito, Y., Prinz, F. High ionic conductivity in ultrathin nanocrystalline gadolinia-doped ceria films. *Applied Physics Letters* **89** 143107 (2006).
- [16] Rossignol, C., Roman, B., Benetti, G.D., Djurado, E. Elaboration of thin and dense CGO films adherent to YSZ by electrostatic spray deposition for IT-SOFC applications. *New J. Chem.* **35** 716-723 (2011).
- [17] Acharya, S. A., Singh, K., Bhoga, S. S. Synthesis and Characterization of Nanosized Dy-Doped of Ceria Developed by Microwave Assisted Combustion Route. *Integrated Ferroelectrics: An International Journal* **121** 13-23 (2010).
- [18] Bae, H., Choi, J., Choi, G.M. Electrical conductivity of Gd-doped ceria film fabricated by aerosol deposition method. *Solid State Ionics* **236** 16-21 (2013).

-
- [19] Wu, H. M., Tu, J. P., Yang, Y. Z. & Shi, D. Q. Spray-drying process for synthesis of nanosized LiMn₂O₄ cathode. *Journal of Materials Science* **41** 4247-4250 (2006).
- [20] Van Driessche, I., Schoofs, B., Bruneel, E. & Hoste, S. The effect of processing conditions on the properties of spray dried Nd₁Ba₂Cu₃O_y/Ag composite superconductors. *Journal of the European Ceramic Society* **24** 1823-1826 (2004).
- [21] Sharma, V., Crozier, P. A., Sharma, R. & Adams, J. B. Direct observation of hydrogen spillover in Ni-loaded Pr-doped ceria. *Catalysis Today* **180**, 2-8 (2012).
- [22] Lundberg, M., Wang, H.-J., Blennow, P. & Menon, M. Mesoporous high surface area Ce_{0.9}Gd_{0.1}O_{1.95} synthesized by spray drying. *Ceramics International* **37**, 797-802 (2011).
- [23] Blennow, P., Chen, W., Lundberg, M. & Menon, M. Characterization of Ce_{0.9}Gd_{0.1}O_{1.95} powders synthesized by spray drying. *Ceramics International* **35**, 2959-2963 (2009).
- [24] Giannuzzi, L.A., Stevie, F.A. Introduction of Focused Ion Beam: Instrumentation, Theory, Techniques and Practice. Springer, 2005.
- [25] Maintained by Klein, A., Reilink, R. <http://www.pyzo.org>.
- [26] Esposito, V., Traversa, E. Design of Electroceramics for Solid Oxide Fuel Cell Applications: Playing with Ceria. *Journal of the American Ceramic Society* **91** 1037-1051 (2008).
- [27] Waldhäusl, J., Preis, W., Sitte, W. Electrochemical characterization of gadolinia-doped ceria using impedance spectroscopy and dc-polarization. *Solid State Ionics* **225** 453-456 (2012).
- [28] Jasper, A. Kilner, J.A., McComp, D.W. TEM and impedance spectroscopy of doped ceria electrolytes. *Solid State Ionics* **179** 21-26 (2008).

-
- [29] Guo, X., Sigle, W., Maier, J. Blocking Grain Boundaries in Yttria-Doped and Undoped Ceria Ceramics of High Purity. *Journal of the American Ceramics Society* **86** 77-87 (2003).
- [30] Ahn, C.C., Krivanek, O.L., EELS Atlas. Pleasanton: Gatan Inc., 1983. Print
- [31] Egerton, R. blah bal.
- [32] Williams, D.B., Carter, C.B., Transmission Electron Microscopy Part 4: Spectrometry. New York: Springer, 2009. Print.
- [33] Lei, Y., Jung, H.J., Browning, N.D. Segregation Effects at Grain Boundaries in Fluorite-Structured Ceramic, *Journal of the American Ceramic Society* **85** [9] 2359-2363 (2002).
- [34] Lee, W., Jung, H.J., Lee, M.H., Kim, Y.-B., Park, J.S., Sinclair, R., Prinz, F.B. Oxygen Surface Exchange at Grain Boundaries of Oxide Ion Conductors. *Advanced Functional Materials* **22** 965-971 (2012).
- [35] Hojo H., et al., Atomic Structure of a CeO₂ Grain Boundary: The Role of Oxygen Vacancies. *Nano Letters* **10** 4668-4672 (2010).
- [36] Stefanik, Todd Stanley. Electrical properties and defect structures of praseodymium-cerium oxide solid solutions. *Diss. Massachusetts Institute of Technology*, 2003.